Genes & Diseases (2022) 9, 1301–1314

Available online at www.sciencedirect.com

ScienceDirect

journal homepage: http://ees.elsevier.com/gendis/default.asp

FULL LENGTH ARTICLE

Defective claudin-10 causes a novel variation of HELIX syndrome through compromised tight junction strand assembly

Sebastian Sewerin [a], Jörg Piontek [b,], Ria Schönauer [a], Sonja Grunewald [c], Angelika Rauch [d], Steffen Neuber [e], Carsten Bergmann [e,f], Dorothee Günzel [b,**,1], Jan Halbritter [a,*,1]**

[a] *Division of Nephrology, University of Leipzig Medical Center, Leipzig 04103, Germany*
[b] *Clinical Physiology/ Nutritional Medicine, Charité – Universitätsmedizin Berlin, Berlin 12203, Germany*
[c] *Division of Dermatology, Venereology, and Allergology, University of Leipzig Medical Center, Leipzig 04103, Germany*
[d] *Division of Prosthodontics and Materials Science, University of Leipzig Medical Center, Leipzig 04103, Germany*
[e] *Center for Human Genetics, Bioscientia, Ingelheim 55218, Germany*
[f] *Medizinische Genetik Mainz, Limbach Genetics, Mainz 55128, Germany*

Received 22 December 2020; received in revised form 1 June 2021; accepted 7 June 2021
Available online 13 July 2021

KEYWORDS
Claudin-10;
HELIX syndrome;
Paracellular transport;
Salt-losing tubulopathy;
Tight junction

Abstract Formation of claudin-10 based tight junctions (TJs) is paramount to paracellular Na^+ transport in multiple epithelia. Sequence variants in *CLDN10* have been linked to HELIX syndrome, a salt-losing tubulopathy with altered handling of divalent cations accompanied by dysfunctional salivary, sweat, and lacrimal glands. Here, we investigate molecular basis and phenotypic consequences of a newly identified homozygous *CLDN10* variant that translates into a single amino acid substitution within the fourth transmembrane helix of claudin-10. In addition to hypohidrosis (H), electrolyte (E) imbalance with impaired urine concentrating ability, and hypolacrimia (L), phenotypic findings include altered salivary electrolyte composition and amelogenesis imperfecta but neither ichthyosis (I) nor xerostomia (X). Employing cellular

* Corresponding author. Division of Nephrology, University of Leipzig Medical Center, Liebigstraße 20, 04103 Leipzig, Germany. Fax: +49 341 97 13389.
** Corresponding author. Clinical Physiology/ Nutritional Medicine, Charité – Universitätsmedizin Berlin, Hindenburgdamm 30, 12203 Berlin, Germany. Fax: +49 30 450 514962.
E-mail addresses: joerg.piontek@charite.de (J. Piontek), dorothee.guenzel@charite.de (D. Günzel), jan.halbritter@medizin.uni-leipzig.de (J. Halbritter).
Peer review under responsibility of Chongqing Medical University.
[1] These authors contributed equally.

https://doi.org/10.1016/j.gendis.2021.06.006

TJ reconstitution assays, we demonstrate perturbation of *cis*- and *trans*-interactions between mutant claudin-10 proteins. Ultrastructures of reconstituted TJ strands show disturbed continuity and reduced abundance in the mutant case. Throughout, both major isoforms, claudin-10a and claudin-10b, are differentially affected with claudin-10b showing more severe molecular alterations. However, expression of the mutant in renal epithelial cells with endogenous TJs results in wild-type-like ion selectivity and conductivity, indicating that aberrant claudin-10 is generally capable of forming functional paracellular channels. Thus, mutant proteins prove pathogenic by compromising claudin-10 TJ strand assembly. Additional *ex vivo* investigations indicate their insertion into TJs to occur in a tissue-specific manner.

Introduction

Recently, sequence variants in *CLDN10* have been linked to a non-Bartter, non-Gitelman salt-losing tubulopathy with altered handling of divalent cations accompanied by dysfunctional salivary, sweat, and lacrimal glands.[1–5] The acronym HELIX has been coined for the associated clinical syndrome encompassing hypohidrosis, electrolyte imbalance, lacrimal gland dysfunction, ichthyosis, and xerostomia.[3] *CLDN10* encodes the tight junction (TJ) protein claudin-10 which comes in two major isoforms, claudin-10a and claudin-10b.[6,7] While the expression of claudin-10a is restricted to kidney and uterus, claudin-10b has been found in many epithelia.[6,7] In the kidney, claudin-10 is expressed by tubular epithelial cells from the proximal convoluted tubule to the cortical thick ascending limb of Henle's loop (TAL) with claudin-10a found in the proximal tubule and claudin-10b expressed along TAL segments.[8]

Claudin-10 belongs to the family of claudins that are integral components of TJs and largely determine their sealing and permeability properties.[9] These proteins share a common topology of four transmembrane helices from which two extracellular loops protrude into the paracellular cleft, forming an extracellular domain.[10] Claudins assemble both in *cis* (within one membrane) and in *trans* (between adjacent cells) to form intramembranous strands and networks thereof that vary in complexity, continuity, and depth.[11] The extracellular domains of claudins critically contribute to strand formation and mediate molecular barrier or selective channel formation, thereby directing the paracellular transport of ions, uncharged solutes, and water.[12–14]

The differential expression of claudin-10 isoforms along the kidney tubule has major implications for the ion selectivity of the paracellular pathway. While claudin-10a is thought to mediate paracellular Cl^- reabsorption in the proximal tubule,[15] claudin-10b complements transcellular Na^+ reabsorption in the TAL by allowing for its paracellular passage due to a lumen-positive transepithelial potential. In this way, in the TAL, half of the total amount of Na^+ is reabsorbed via the paracellular route. In glandular physiology, claudin-10b appears to play an even more critical role in saliva, sweat, and tear secretion as it is thought to mediate all of the transepithelial Na^+ transport.[2,3]

Here, we investigate phenotypic features, molecular consequences, and renal pathophysiology associated with a novel homozygous *CLDN10* missense variant. Besides an expansion of the HELIX phenotype we provide evidence of defective TJ strand assembly accounting for altered paracellular ion transport.

Methods

For comprehensive methods, see Supplementary Methods.

Study approval

Patient data and material were used following approval (#402/16-ek) of the institutional review board (#IRB00001750) at University of Leipzig Medical School. Written informed consent was obtained from the patient involved in this study, including the consent to publish patient photographs. From healthy controls for diuretics responsiveness testing (4 males and 1 female, aged 30.8 ± 4.6 years, mean $\pm$ SD), written informed consent to participate was obtained prior to the study.

Genetic analysis

Genomic DNA was extracted from whole blood, analyzed with next generation sequencing technology using Illumina sequencing-by-synthesis technology and bioinformatically interpreted as described before.[16] Details are provided in Supplementary Methods. The reported homozygous *CLDN10* variant was confirmed by Sanger sequencing. Copy number variation analysis did not suggest hemizygosity.

Clinical testing

Diuretics responsiveness tests were based upon a previously published protocol.[17] Water deprivation and hypertonic saline infusion tests were essentially performed as previously described.[18] Details and further clinical tests are described in Supplementary Methods. We remark that the patient was 18 or 20 years of age when clinical tests were performed.

Immunofluorescence and immunohistochemistry

Immunofluorescence and immunohistochemical labeling of TJ components was performed as detailed in Supplementary Methods.

Structural bioinformatics and molecular modeling

Homology models were created utilizing MODELLER[19] and Schrödinger's BioLuminate/Maestro (Biologics Suite, Release 2019-2, Schrödinger, Germany). For the claudin-10b protomer model, the claudin-15 crystal structure[20] (PDB ID 4P79) was used as template. For the claudin-10a protomer model, the claudin-10b model was used as template. Images were created with PyMOL 2.3 (Schrödinger, Germany).

CLDN10 expression constructs, cell culture, and transfection

CLDN10 expression constructs were generated and HEK293 and MDCK-C7 cells were cultured and transfected as detailed in Supplementary Methods.

Förster resonance energy transfer (FRET) assay

FRET was assessed between CFP- and YFP-claudin fusion proteins in transiently transfected HEK293 cells essentially as previously reported.[21] A description can be found in Supplementary Methods.

Freeze-fracture electron microscopy

Stably transfected HEK293 cells were grown in 6-well plates until confluency and processed for freeze-fracture electron microscopy as previously reported.[22] For quantification of strand breaks, electron micrographs were analyzed as detailed in Supplementary Methods.

Electrophysiology

Dilution and biionic potential measurements in stably transfected MDCK-C7 cell layers were essentially carried out as previously described.[7] Liquid junction potentials were corrected for as previously reported.[23] Relative permeabilities were computed as detailed in Supplementary Methods. Pore diameter was estimated by plotting the square root of P_X/P_{Na} (X, NH_4^+ and various organic cations) against cation diameters and extrapolating the linear part of the relationship.[23]

Results

Clinicals

A 16-year-old male of consanguineous Afghan descent presented with nocturnal enuresis, polyuria, and polydipsia since early childhood. Upon clinical examination, arterial hypotension and bradycardia were noted. Beard growth and axillary hair were markedly reduced while ichthyosis was not evident on dermal inspection. Laboratory tests revealed marked hypochloremic alkalosis with hypokalemia as well as high serum renin and aldosterone levels (Table S1). Additionally, hypermagnesemia and hypocalciuria were evident. Serum creatinine was normal and there were no morphological abnormalities on renal ultrasound, especially no signs of nephrocalcinosis or nephrolithiasis.

Genetic testing

Genetic testing by means of a tubulopathy specific gene panel revealed a novel homozygous missense variant in *CLDN10* (c.494G>C; NM_006984.4). Consequences at the protein level are p.(Gly163Ala) for claudin-10a and p.(Gly165Ala) for claudin-10b, henceforth referred to as G163A and G165A, respectively. G163/G165 is located within the fourth transmembrane helix of claudin-10a/b and is highly conserved across species and among claudin family members (Fig. S1). Absence of the variant in both mutation (HGMD, ClinVar) and population databases (gnomAD, ExAc) as well as recent reports of claudin-10 associated disease[1–4] suggested pathogenicity. Unfortunately, additional family members were unavailable for segregation analysis.

Assessment of renal tubular pathophysiology

To further characterize underlying mechanisms of enuresis, polyuria, and polydipsia, we performed diuretics responsiveness testing. Blocking the Na^+-Cl^--cotransporter in the proximal part of the distal convoluted tubule by hydrochlorothiazide led to an exaggerated response of fractional Na^+ and Cl^- excretions (ΔFE_{Na} 8.40% and ΔFE_{Cl} 13.65%, respectively, with Δ signifying maximal increase over mean basal level), resembling that observed in Bartter syndrome type I.[17] Loop diuretic responsiveness testing revealed no overt differences in increases of fractional Na^+ and Cl^- excretions between patient and controls (Fig. 1A, S2). Assuming complete blocking of TAL paracellular Na^+ transport, this is compatible with partial compensation by the transcellular pathway. Additionally, a profound effect on renal Mg^{2+} and K^+ handling was evident. While an exaggerated response of fractional Mg^{2+} excretion in the patient is suggestive of enhanced TAL paracellular Mg^{2+} reabsorption, the loop diuretic effect on fractional K^+ excretion is compatible with adaptive changes in the distal nephron promoting enhanced K^+ secretion with an increase in NaCl delivery.

Urine concentrating ability was assessed during water deprivation and turned out to be markedly reduced with urine osmolalities remaining below 600 mosmol/kg (Fig. 1B). Administration of desmopressin, an analogue of arginine vasopressin (AVP), resulted in an increase of urine osmolality of less than 10%. Determination of hypertonic saline-stimulated serum copeptin (25.3 pmol/L) indicated no defect in central AVP release,[18] as did basal copeptin levels (12.5 $\pm$ 3.5 pmol/L, mean $\pm$ SD, $n = 3$).[24] In the absence of a compensatory increase in endogenous AVP release,[24,25] both compromised urine concentrating capacity and limited renal response to desmopressin most likely reflect a reduction in the buildup of medullary

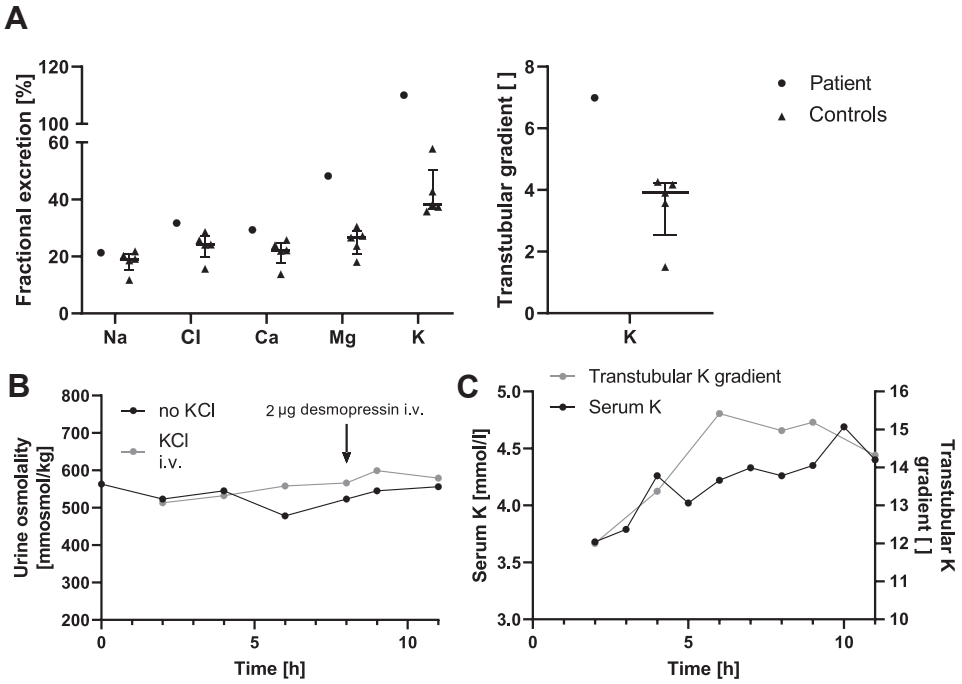

Figure 1 Assessment of renal phenotype. (**A**) Furosemide responsiveness testing in the patient and in 5 control subjects. Shown are maximal absolute initial changes during loop diuretic exposition over mean basal levels. The transtubular K^+ concentration gradient (TTKG) was defined as urinary K^+/serum K^+ whenever serum osmolality exceeded urinary osmolality and else was calculated from the standard formula.[27] Overt differences between the patient and controls are observed only for fractional excretions of Mg^{2+} and K^+ as well as for the TTKG. The loop diuretic effect on fractional Mg^{2+} excretion signifies that paracellular Mg^{2+} reabsorption in the thick ascending limb of Henle's loop is enhanced in the patient and may be involved in the development of hypermagnesemia. Loop diuretic effects on fractional K^+ excretion can be explained by adaptive changes in the distal nephron promoting enhanced K^+ secretion upon an increase in NaCl delivery. Median and IQR. (**B**) Development of urine osmolality in the patient over time during water deprivation with and without administration of KCl. Results are similar for both tests and indicate a markedly reduced urine concentrating ability with a blunted response to desmopressin, irrespective of an increase in serum K^+ level. (**C**) In the patient, the increase in serum K^+ parallels that of TTKG during water deprivation with concomitant intravenous KCl substitution. i.v., intravenously.

interstitial osmolality. In order to assess the impact of short-term increases in serum K^+ on maximal urine concentration while bypassing any gut-mediated kaliuretic effects,[26] water deprivation testing was repeated with continuous intravenous infusion of KCl. Raising serum K^+ by about 1 mmol/L did neither impact urine osmolality nor desmopressin responsiveness (Fig. 1B). Yet, activity of the distal nephron K^+ secretory process as determined by transtubular K^+ concentration gradients[27] rose with serum K^+ levels (Fig. 1C).

Assessment of extrarenal manifestations

Given the vast bodily distribution of claudin-10b and its significance for proper functioning of several exocrine glands,[28] we sought to define the extrarenal phenotype.

Stimulated saliva flow rates did not differ between patient and controls (Fig. 2A). Yet, measurements of electrolytes in salivary fluid revealed pronounced ion imbalances in the patient (Fig. 2B): Na^+ and Cl^- levels were markedly lower than in controls, compatible with the critical role of paracellular Na^+ transport for NaCl secretion in glandular epithelia.[28] On the contrary, K^+ levels were exceedingly high, while Ca^{2+} contents were unaltered. Immunofluorescence labeling of claudin-10 in submucosal salivary glands from the labial mucosa revealed a complete absence of the protein in comparison with control tissue that showed clear staining (Fig. 2C, S3).

Notably, despite the absence of xerostomia, severe enamel wear was found clinically and radiographically (Fig. 2D, E), suggesting impaired amelogenesis.

Schirmer's test was used to assess tear production and revealed bilateral hypolacrimia (Fig. 3A).

The starch-iodine test was used to qualitatively assess sweat secretion. Results were compatible with generalized hypohidrosis with the axillae more severely affected than palmar and plantar aspects of hands and feet, respectively (Fig. 3B). Quantitative assessment of sweat secretion indicated reduced basal and stimulated axillary sweat secretion rates (Fig. 3C). Immunohistochemical staining of axillary skin biopsy specimens showed the presence of claudin-10 in secretory tubules of eccrine sweat glands in both patient and control samples (Fig. 3D, E). Similarly, immunofluorescence labeling of claudin-10 in eccrine sweat glands demonstrated its presence in canaliculi of secretory portions (Fig. 3F).

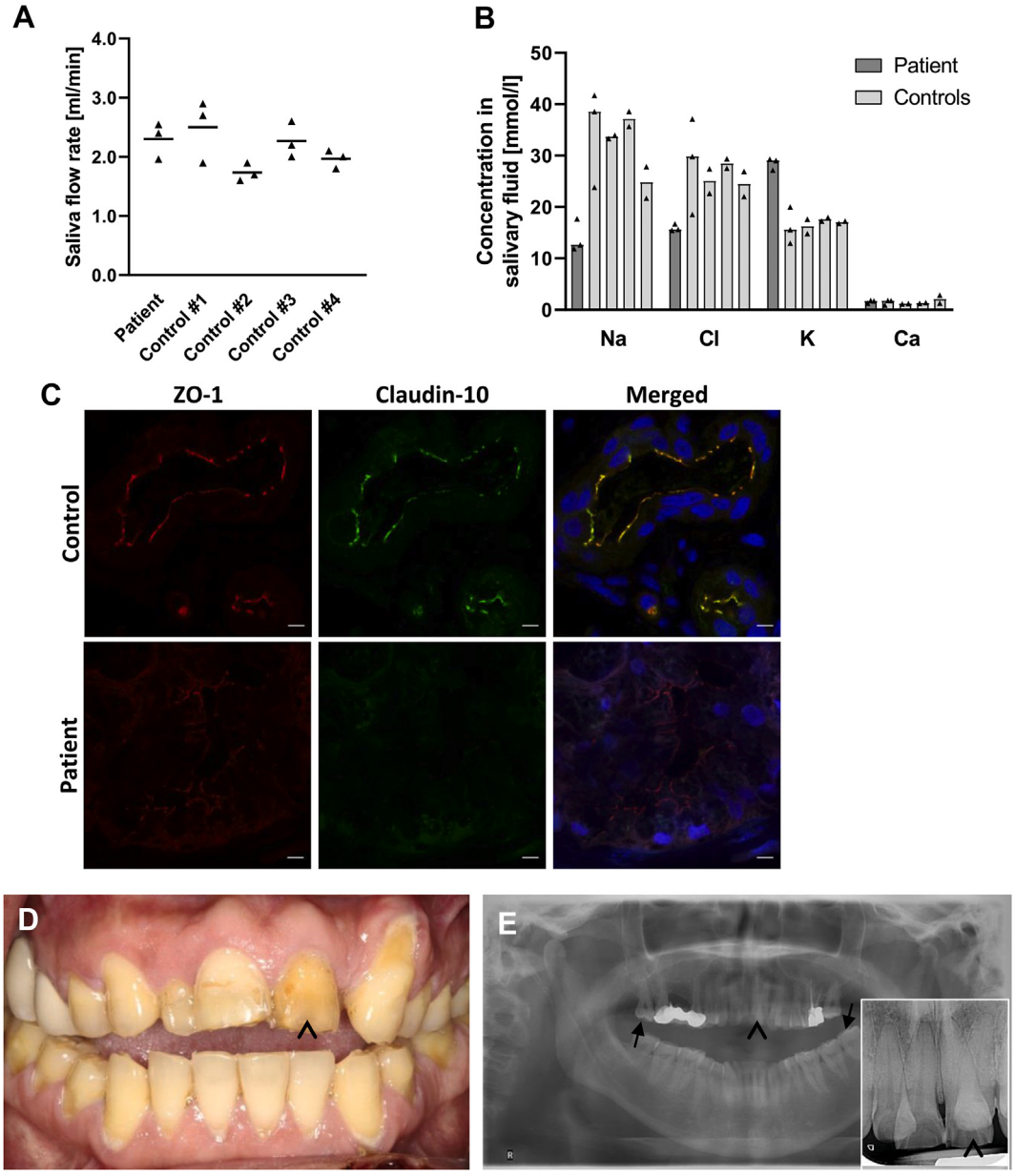

Figure 2 Assessment of dental phenotype and saliva secretion. (**A**) Stimulated saliva flow rates in the patient and in 4 control subjects. The amount of saliva produced did not differ between the patient and controls. Mean. (**B**) Assessment of Na^+, Cl^-, K^+, and Ca^{2+} concentrations in salivary fluid from the patient and from 4 control subjects. While Na^+ and Cl^- concentrations were markedly lower in the patient, K^+ levels were exceedingly high. Ca^{2+} concentrations turned out to be comparable between the patient and control subjects. Median. (**C**) Immunofluorescence labeling of claudin-10 and ZO-1 in submucosal salivary glands from the labial mucosa. When compared with control tissue, a complete absence of claudin-10 and a weaker ZO-1 signal are evident in the patient. Nuclei are stained with DAPI (blue). Scale bars, 5 μm. (**D**,**E**) Dental findings in the patient. Both clinical view and radiographs demonstrate severe enamel wear of the permanent teeth especially in the anterior region (arrowheads). Note the anteriorly open bite which is frequently associated with amelogenesis imperfecta[41] and makes enamel wear unlikely to result from bruxism. On radiographs, enamel is still evident on molar teeth (arrows).

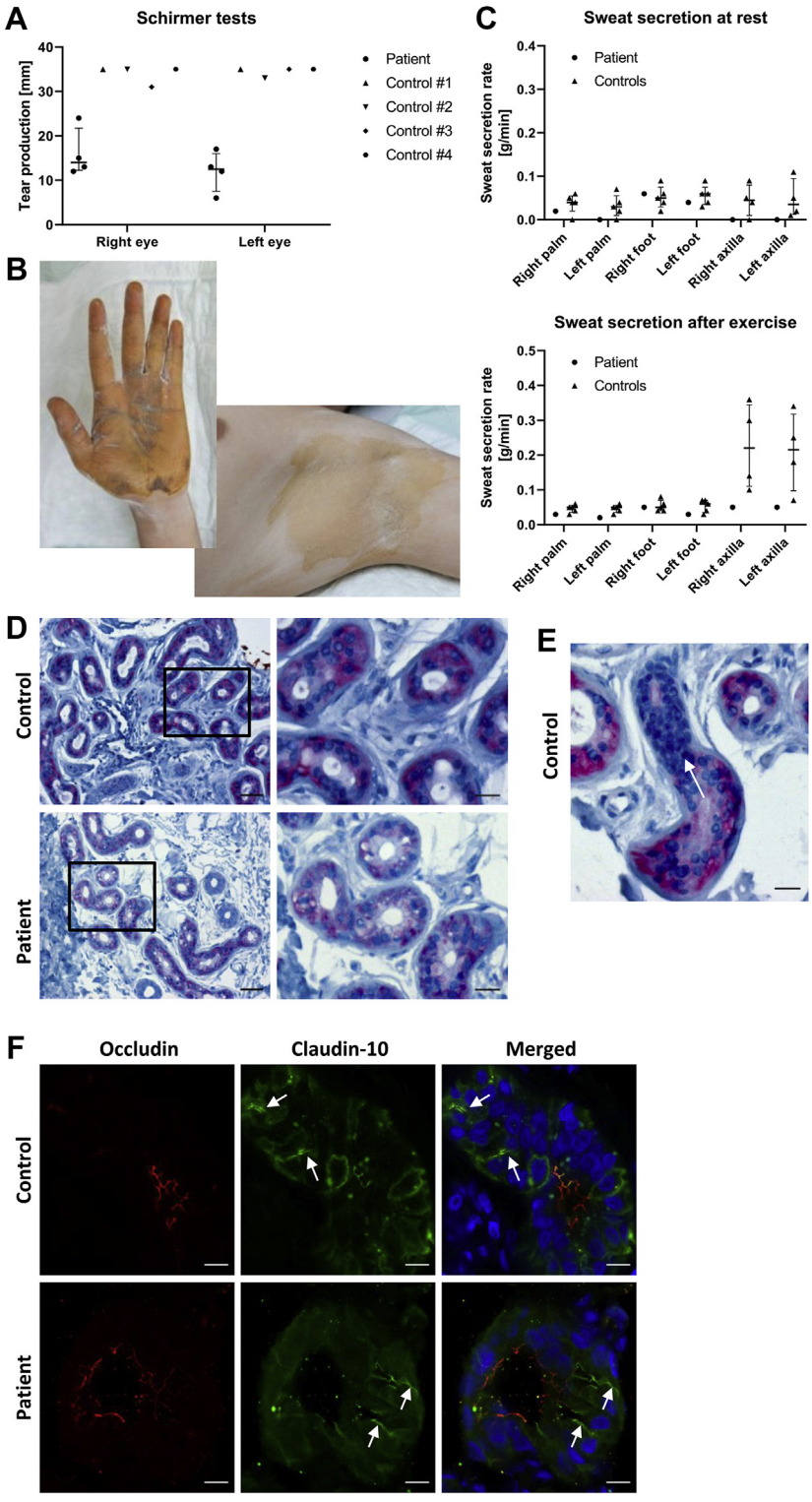

Figure 3 Assessment of tear production and sweat secretion. (**A**) Tear production as assessed by Schirmer's test in the patient and in 4 control subjects. Results demonstrate bilateral hypolacrimia in the patient. Median and IQR. (**B**) Exemplary images from starch-iodine test in the patient. The starch-iodine reaction does only occur in the presence of water, indicated by dark discoloration. Axillae are more severely affected from hypohidrosis than palmar aspects of hands. (**C**) Quantitative assessment of sweat secretion before and after exercise in the patient and in 5 control subjects, indicating reduced basal and stimulated sweat secretion rates in both patient axillae. Median and IQR. (**D,E**) Immunohistochemical staining of claudin-10 in axillary skin biopsy specimens. In patient and control samples, claudin-10 (pink) is well-detectable and localizes to secretory tubules of eccrine sweat glands but is not found in excretory ducts (nuclei in dark blue). (**D**) Scale bars, 50 μm (left column) or 20 μm (right column). (**E**) demonstrates the loss of claudin-10 expression as a secretory tubule merges into an excretory duct (arrow) in a control

Homology modeling of claudin-10 3D structures and oligomerization

To assess the variant's impact on tertiary protein structures, we employed homology modeling of human claudin-10 based upon claudin-15 crystal structure[20] and previously reported claudin-10b models.[13] In the resulting claudin-10a/-10b models, G163/G165 points to the center of the transmembrane four-helix bundle (Fig. 4A–C, E). This glycine residue is strongly conserved among claudins (Fig. S1),[14] indicating that its small size and great torsional angle space are important for tight conformational packing of the four-helix bundle which is challenged by the insertion of a methyl group in the G163A/G165A variant (Fig. 4D, F). The models further indicate that the substitution G165A in claudin-10b is less well tolerated than G163A in claudin-10a because of the larger sidechain of T24 in claudin-10b which corresponds to A22 in claudin-10a. Additionally, data available for the region surrounding G163/G165 support the idea that G163A/G165A directly affects claudin-10 conformation (Fig. 4B).

As G165 does not line an interface between claudin protomers (Fig. 4G, H), we propose G165A (and, to a lesser extent, G163A in claudin-10a) to indirectly affect claudin assembly by perturbing the transmembrane four-helix bundle. Underlying mechanisms might involve alterations of the *cis*-interface close by, slight repositioning of W30 and the extracellular β-sheet involved in *cis*- and *trans*-interactions, or alterations of the membrane environment between claudin protomers (Fig. 4G, H).[13]

Assessment of *trans*-interaction capability of wild-type and mutant claudin-10

To analyze claudin oligomerization, a TJ strand reconstitution assay was performed. YFP tagged claudin-10 proteins were transiently overexpressed in HEK293 cells (Fig. 5A). As these cells do not contain endogenous TJs, alterations in *de novo* formation of claudin-10 TJ strands could be probed in this way. Both YFP-claudin-10a wild-type (WT) and G163A showed similar enrichment at cell-cell contacts. In addition, they prominently localized to non-acidic intracellular granules in a similar fashion (Fig. S4). Also, YFP-claudin-10b WT localized to the cell membrane with strong enrichment at cell-cell contacts, indicating *trans*-interactions and TJ strand formation. In contrast, YFP-claudin-10b G165A appeared to be more evenly distributed across the surface of neighboring cells, even though enrichment at cell-cell contacts was found to some extent. The lack of prominent enrichment indicates perturbed *trans*-interactions between claudin-10b G165A proteins. These data were supported by quantification of claudin-10 enrichment at individual cell-cell contacts, showing significantly lower enrichment factors for claudin-10b G165A when compared with the corresponding wild-type (Fig. 5B). We conclude that *trans*-interaction properties of both claudin-10 isoforms are differentially affected by the mutation.

Assessment of *cis*-interaction properties of wild-type and mutant claudin-10

For analysis of claudin *cis*-interaction, a FRET based cellular assay was employed.[22,29] To probe the spatial *cis*-proximity between claudins, we assessed FRET efficiencies at cell-cell contacts between HEK293 cells coexpressing different CFP- and YFP-claudin fusion proteins that functioned as FRET-donor/-acceptor pairs (Fig. 5C). In the case of claudin-10a, FRET efficiencies were reduced only when assessing the interaction between claudin-10a G163A proteins. Coexpression of claudin-10a WT led to a complete rescue of proper *cis*-interactions. For claudin-10b, results indicate perturbed *cis*-interactions between claudin-10b G165A and both claudin-10b WT and G165A with a partial rescue by coexpression of the wild-type, indicating that the mutation's impact on claudin-10 function is more severe for claudin-10b. Thus, G163A/G165A perturbs *cis*-interactions between claudin-10a/b proteins in reconstituted TJ strands.

Subcellular distribution of exogenous wild-type and mutant claudin-10 in MDCK-C7 and HEK293 cells

Differentiated renal epithelial cells (MDCK-C7) were stably transfected with wild-type and mutant claudin-10 constructs. Note that endogenously, MDCK-C7 cells express claudin-1, -3, -4, -5, -7, and -8 but no claudins that are known to form paracellular channels such as claudin-10a or claudin-10b.[30–32] Immunofluorescence labeling of claudin-10 showed membrane localization and varying degrees of intracellular accumulation (Fig. S5). While mutant proteins exhibited clear staining in a mottled perinuclear pattern, these effects were markedly less pronounced in claudin-10a/b WT expressing cells. For claudin-10b, these findings were corroborated by the fact that relative amounts of tight junctional claudin-10 were reduced in the mutant case (Fig. S6). In contrast, when transiently overexpressed in HEK293 cells, both claudin-10a WT and G163A localized in the cell interior to non-acidic granules while claudin-10b WT and G165A showed no notable intracellular accumulation (Fig. 5A, S4). These differential findings may reflect tissue-specificity of the cellular processing of aberrant claudin-10.

Ultrastructures of wild-type and mutant claudin-10 TJ strands

Freeze fracture electron microscopy was employed to analyze the ultrastructure of TJ strands reconstituted by stable expression of *CLDN10* constructs in HEK293 cells. In cells expressing either claudin-10a or claudin-10b WT, regular meshworks of continuous TJ strands were detected on the proto- (P-) and exoplasmic (E-) faces of the plasma membrane (Fig. 6A, D, E), as was shown previously.[22] In the case of claudin-10a G163A, TJ strands were frequently found to be discontinuous, consisting of beaded particles on the P-face (Fig. 6B, C), which indicates altered TJ strand

specimen. Scale bar, 20 μm. (**F**) Immunofluorescence labeling of secretory tubules from eccrine sweat glands. In both patient and control samples, claudin-10 predominantly localizes to canaliculi (arrows), whereas occludin localizes to membranes lining the lumen and is found in canaliculi to a lesser extent. Nuclei are stained with DAPI (blue). Scale bars, 10 μm.

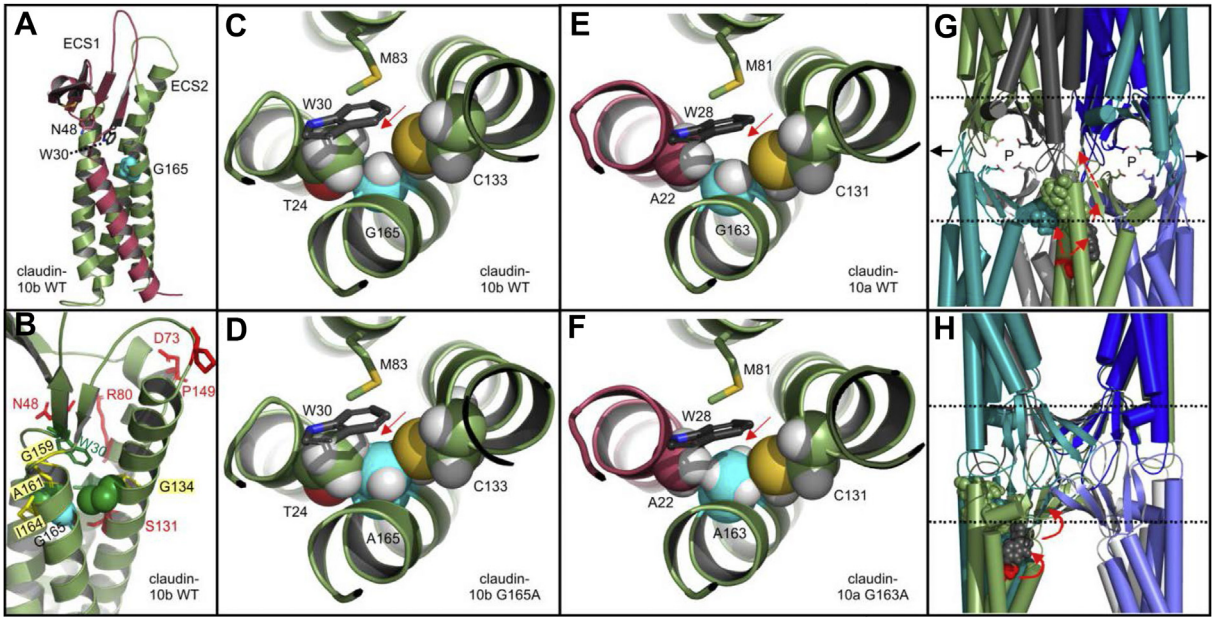

Figure 4 Homology models of claudin-10 3D-structures. (**A**–**C**) Claudin-10b WT model (cartoon, based upon claudin-15 template,[20] PDB ID 4P79). (**A**) G165 (cyan spheres) points to the center of the extracellular half of the transmembrane four-helix bundle. Claudin-10a and -10b differ in the sequence of transmembrane helix (TM) 1 and extracellular loop/segment (ECS) 1 (dark red). W30 and N48 (shown as sticks) are part of the W-G/NLW-C-C claudin consensus motif[42] with W30 being important for anchoring the ECS1/2 β-sheet to the transmembrane four-helix bundle[20] and N48 differing between claudin-10a and -10b. (**B**) Different perspective on claudin-10b WT model. Residues T24 and C133 are shown as green spheres. Shown as red sticks are residues mutations of which cause HELIX syndrome. G134, G159, A161, and I164 (yellow sticks) correspond to positions that have been implicated in structure and function of other claudins. (**C**) Close-up, top view. G165 (cyan, white spheres) is surrounded by T24 and C133 (spheres), W30 and M83 (sticks). Atoms: O, red; S, yellow; N, blue; H white. (**D**) Close-up of claudin-10b G165A model. The insertion of a methyl group (red arrow) causes steric conflicts (overlap) between A165 and both T24 and C133. (**E**) Close-up of claudin-10a WT model. As TM1 (dark red) differs between claudin-10a and -10b, amino acid positions in claudin-10a are shifted by 2 with respect to claudin-10b. G163 (cyan, white spheres) is surrounded by A22 and C131 (spheres), W28 and M81 (sticks). (**F**) Close-up of claudin-10a G163A model. Compared with T24 in claudin-10b, A22 of claudin-10a lacks a hydroxyl group and is smaller in size, causing only minor steric conflicts between A163 and both A22 and C131. The model predicts the mutation to be less well tolerated in claudin-10b when compared with claudin-10a. (**G, H**) Model of polymeric claudin-10b tight junction strand containing ion channels (adapted from Hempel et al 2020[13]). Octamer with claudin-10b protomers shown in different colors as simplified cartoon. Membrane surfaces (dashed lines), paracellular ion pores (P) with charge selectivity mediating D56 residues (sticks) and polymeric expansions (black arrows) are indicated. G165 (red spheres) is not located at an interface between claudin protomers (note the gaps between cyan and green protomers in (G) and between green and marine protomers in (H, model turned by 90°)). G165A might indirectly affect (red arrows) *cis*-interfaces (cyan, green spheres) or *trans*-interfaces by potentially affecting W30 (black spheres) and in turn the ECS β-strands' positioning involved in claudin assembly.[13] For additional details, see Supplementary Information on Figure 4. WT, wild-type.

assembly. Claudin-10b G165A strands were altered even more drastically with highly discontinuous and fragmented TJ strands on both P- and E-faces (Fig. 6F, G). Quantitatively, the proportion of gaps along strands was significantly higher in the mutant cases when compared with the respective wild-types (Fig. 6H). This held also true for claudin-10b G165A strands compared with claudin-10a G163A strands. Additionally, strand abundance appeared to be reduced in both mutant isoforms, an effect more pronounced for claudin-10b G165A. Thus, for both mutants, TJ strand formation is compromised with claudin-10b strands being more severely affected by the mutation.

Dilution and biionic potential measurements

In order to determine whether the mutation affects paracellular channel selectivity, we investigated NaCl dilution potentials and biionic potentials for monovalent cations in MDCK-C7 cell layers stably transfected with wild-type and mutant claudin-10 constructs. Given their endogenous claudin expression pattern, MDCK-C7 monolayers are characterized by high transepithelial resistance and the lack of charge preferences of the paracellular pathway, hence constituting a standard expression system for functional analyses of channel forming claudins.[30–32] Permeability ratios of Cl^- and Na^+ turned out to be comparable ($P_{Cl}/P_{Na} > 1$) between claudin-10a WT and G163A expressing cell layers (Fig. 7A). Similarly, mutant claudin-10b retained the wild-type preference for Na^+ over Cl^- ($P_{Na}/P_{Cl} > 1$) (Fig. 7B). Thus, the mutation does not affect charge preferences of claudin-10 channels. The absence of overt differences in transepithelial resistance between claudin-10a/b WT and G163A/G165A expressing cell layers with comparable permeability ratios indicated no substantial alteration of

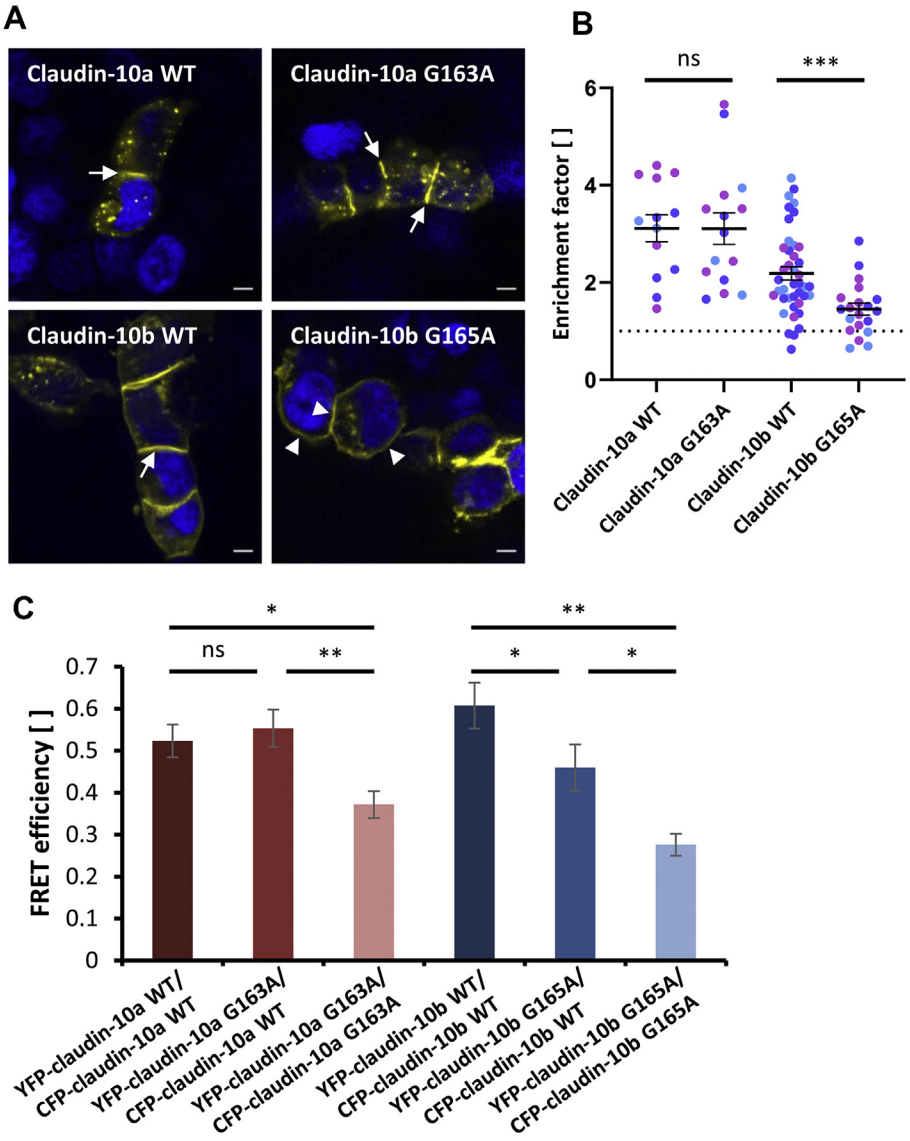

Figure 5 The mutation G163A/G165A differentially affects *trans*- and *cis*-interaction properties of claudin-10 isoforms in tight junction (TJ) strands reconstituted in HEK293 cells. (**A, B**) Cells were transiently transfected with YFP tagged claudin-10 constructs. (**A**) YFP-claudin-10a WT and G163A show similar enrichment at cell-cell contacts between claudin-expressing cells (arrows) and in intracellular granules. Similarly, YFP-claudin-10b WT shows strong contact enrichment (arrow), indicating *trans*-interactions and TJ strand formation. In contrast, YFP-claudin-10b G165A frequently distributes more evenly across the membranes of neighboring cells (arrowheads), indicating inhibition of *trans*-interactions. Nuclei are stained with DAPI (blue). Representative images from 3 biological replicates; scale bars, 5 μm. (**B**) Enrichment factors computed for individual cell-cell contacts between claudin-expressing cells. Claudin-10b G165A expressing cells show significantly less contact enrichment than cells expressing the corresponding wild-type. In contrast, claudin-10a WT and G163A expressing cells exhibit no significantly different contact enrichment. The dotted line indicates enrichment factor = 1. Enrichment factors >1 are considered to indicate *trans*-interactions. Different colors represent data from different biological replicates ($n = 2–20$ per replicate per condition). Welch's one-way ANOVA with Dunnett's T3 multiple comparisons test; ns, not significant; ***, $P < 0.001$. Mean ± SEM. (**C**) *Cis*-interaction assay using Förster resonance energy transfer (FRET) between CFP- and YFP-claudin-10 fusion proteins transiently coexpressed in HEK293 cells. Mean FRET efficiencies are significantly reduced for both YFP-/CFP-claudin-10a G163A and YFP-/CFP-claudin-10b G165A when compared with the corresponding wild-types. Complete (claudin-10a) or partial (claudin-10b) restoration of FRET efficiencies can be achieved by coexpression of the respective wild-type isoform. Thus, G163A/G165A perturbs *cis*-interactions between claudin-10a/b proteins and coexpression of the respective wild-type rescues *cis*-interactions more efficiently in the case of claudin-10a. One-way ANOVAs followed by two-tailed t-tests with Bonferroni-Holm correction; ns, not significant; **, $P < 0.01$; *, $P < 0.05$. Mean ± SEM ($n = 11–47$). WT, wild-type.

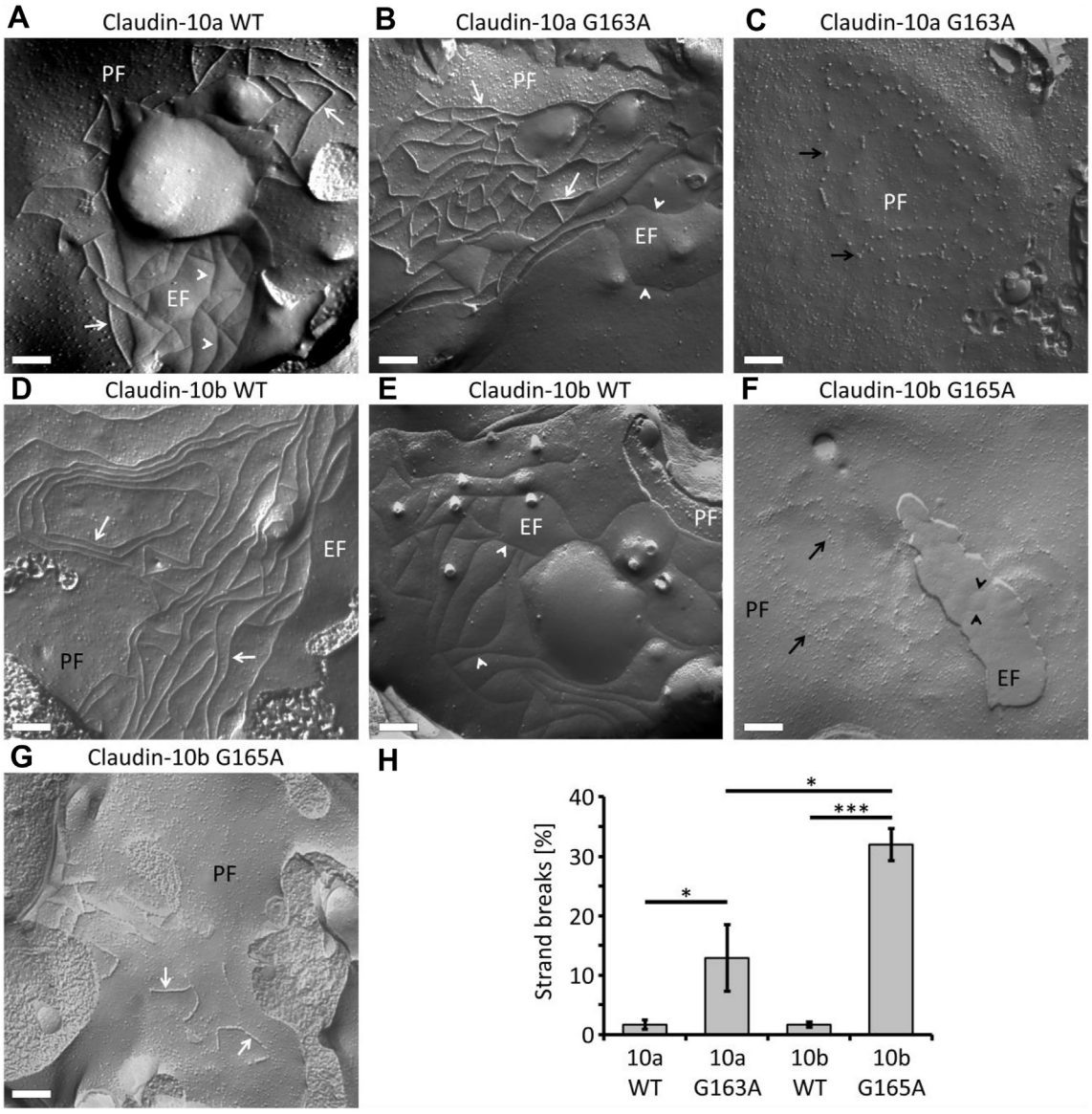

Figure 6 Freeze fracture electron micrograph analysis of HEK293 cells stably expressing claudin-10 constructs. (**A**) Claudin-10a WT forms meshworks of continuous tight junction (TJ) strands (white arrows) detected on the protoplasmic fracture face (PF) of the plasma membrane. On the exoplasmic fracture face (EF), complementary continuous grooves are evident (white arrowheads). (**B**) For claudin-10a G163A, similar continuous TJ strands (white arrows) on the PF and grooves (white arrowheads) on the EF are detected to some extent. (**C**) In most instances, however, discontinuous claudin-10a G163A TJ strands (black arrows) are detected in the form of beaded particles on the PF. The abundance of strands appears to be lower than for claudin-10a WT. (**D, E**) As is the case with claudin-10a WT, claudin-10b WT forms meshworks of continuous TJ strands (white arrows) on the PF and complementary continuous grooves on the EF (white arrowheads). (**F**) In contrast, for claudin-10b G165A, fewer and highly discontinuous, fragmented TJ strands (black arrows) can be detected as beaded particles on the PF. On the EF, irregular grooves, pits, and particles are evident (black arrowheads). (**G**) For claudin-10b G165A, only in few cases, short continuous TJ strands (white arrows) are observed on the PF. Representative images; scale bars, 200 nm. (**H**) Quantification of strand breaks. Percentages of strand breaks are higher in the mutant cases. In addition, claudin-10b G165A strands exhibit higher break percentages than do claudin-10a G163A strands. Along strands, the particle-free distances between particles or strand segments were determined. The percentage of strand breaks was calculated from the quotient total particle-free length/total strand length. For each sample, $n = 10$ electron micrographs were analyzed. Kruskal-Wallis test followed by post-hoc two-tailed Mann Whitney tests with Holm-Šídák multiple comparisons test; *, $P < 0.05$; ***, $P < 0.001$. Mean ± SEM. WT, wild-type.

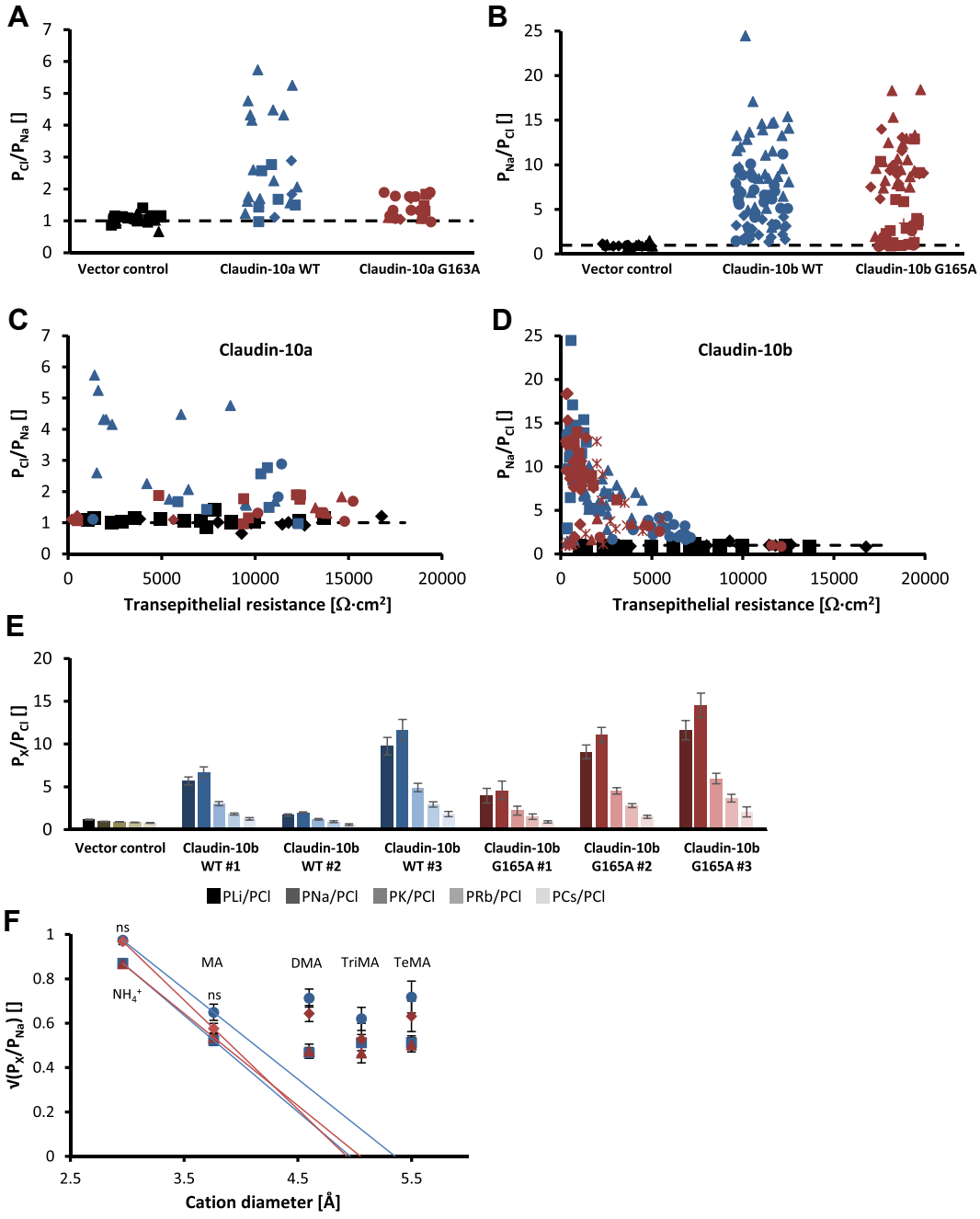

Figure 7 Electrophysiological properties do not differ between claudin-10a/b WT and G163A/G165A expressing MDCK-C7 cell layers. (**A, B**) Permeability quotients as computed from NaCl dilution potentials demonstrate a preservation of charge selectivity in both mutant cases. Paracellular channels reconstituted from claudin-10a G163A retain a preference for Cl^- over Na^+ ($P_{Cl}/P_{Na} > 1$). Paracellular channels reconstituted from claudin-10b G165A favor the permeation of Na^+ over Cl^- ($P_{Na}/P_{Cl} > 1$) as do claudin-10b WT channels. Different symbols represent data from different stably transfected clones. Dashed lines indicate $P_{Na} = P_{Cl}$. (**C, D**) Transepithelial resistance is not overtly different between claudin-10a/b WT and G163A/G165A expressing MDCK-C7 cell layers. Permeability quotients as computed from NaCl dilution potentials are plotted against transepithelial resistance. Different symbols represent data from different stably transfected clones (blue: claudin-10a/b WT, red: claudin-10a/b G163A/G165A, black: vector control). Dashed lines indicate $P_{Na} = P_{Cl}$. (**E**) For both claudin-10b WT and G165A, monovalent cation permeability sequences as computed from biionic potentials correspond to Eisenman sequence X ($Na^+ > Li^+ > K^+ > Rb^+ > Cs^+$). For both claudin-10b WT and G165A, data from three different stably transfected clones (#) are shown. Mean ± SEM (n = 6–13). (**F**) Estimation of paracellular pore diameter from biionic potentials for NH_4^+ and various organic cations. Pore diameters do not differ between claudin-10b WT and G165A (maximally 5 Å). For both claudin-10b WT (blue) and G165A (red), data from two stably transfected clones are shown as indicated by differing symbols (per clone n = 6–11 for NH_4^+, n = 6–8 for MA, n = 6–8 for DMA, n = 3–6 for TriMA, n = 2–6 for TeMA). Two-tailed t-tests; ns, not significant. Square root of mean ± SEM. WT, wild-type; MA, methylammonium; DMA, dimethylammonium; TriMA, trimethylammonium; TeMA, tetramethylammonium.

single channel ion conductivity (Fig. 7C, D). Monovalent cation permeability sequences for claudin-10b WT and G165A expressing cell layers both corresponded to Eisenman sequence X ($Na^+ > Li^+ > K^+ > Rb^+ > Cs^+$), indicating that channel selectivity was unaltered (Fig. 7E). Pore diameter was estimated from biionic potentials for the monovalent cations NH_4^+, methylammonium, dimethylammonium, trimethylammonium, and tetramethylammonium to be identical for both claudin-10b WT and G165A (maximally 5 Å) (Fig. 7F).

Discussion

In this study, we demonstrate pathogenicity of a novel missense variant in *CLDN10* by investigating associated molecular alterations and phenotypic traits. Homology modeling predicted destabilization of the claudin transmembrane four-helix bundle, leading to perturbed oligomerization processes.

Indeed, in HEK293 cells which do not form TJs by themselves, reconstituted mutant claudin-10 TJ strands exhibited defective architecture and compromised protein interaction properties. Ultrastructural analysis of mutant TJ strands showed fragmentation, discontinuity, and reduced abundance. *Cis*-interactions between claudin-10 proteins as probed by the assessment of FRET efficiencies were perturbed in both mutant isoforms. Throughout, claudin-10b G165A displayed more severe alterations than claudin-10a G163A, in line with structural implications from homology modeling. Fluorescence microscopy suggested compromised claudin-10 *trans*-interactions only for claudin-10b G165A. Of note, however, a distinction between a primary *trans*-interaction defect and a merely indirect effect induced by the inhibition of *cis*-interactions cannot be made at this point. Together, the observed defects in claudin-10 interaction properties do well explain the perturbation of TJ architecture evident on electron micrographs by an impairment of TJ strand assembly.

Our electrophysiological findings in MDCK-C7 cells demonstrate that mutant claudin-10 is generally capable of forming paracellular channels with preserved selectivity and conductivity if inserted into pre-existing TJ structures. In line with results from homology modeling, G163A/G165A hence does not affect the pore lining and in turn does not alter the interaction with permeating ions. Instead, the mutation impedes claudin oligomerization and TJ strand assembly which manifests in various ways, depending on cell type or tissue: (i) In HEK293 cells, reconstituted TJ strands are fragmented; (ii) in MDCK-C7 cells and in epithelial cells from secretory tubules of eccrine sweat glands, TJ strands contain functional claudin-10 channels even if absolute claudin-10 abundance at the TJ may be reduced; and (iii) small salivary glands lack claudin-10 altogether.

We conclude that mutant proteins assemble to form functional paracellular channels in a tissue-specific manner which may depend on TJ composition and regulatory factors. In regards to our data we speculate that the specific claudin environment promotes stabilization of mutant claudin-10 in secretory tubules of eccrine sweat glands, yet is unfavorable in those of small salivary glands. Phenotypically, sweat secretion rates were preserved to some extent, whereas the rate of saliva secretion was unaffected but ionic saliva composition showed marked abnormalities. These data indicate diverging roles of claudin-10 in glandular processes of fluid secretion. Given the mosaic pattern of claudin expression in the kidney's TAL with mutual exclusion of claudin-3/-16/-19 and claudin-10 TJs,[33] mutant claudin-10 is not expected to be inserted into TAL TJs. For our patient, this remains elusive in the absence of a kidney biopsy. However, claudin-10 was found to be absent from the TAL of two other HELIX patients.[3,5]

Of note, our data contrast with previous reports of xerostomia in HELIX patients.[2–5,28] However, quantitative assessment of saliva secretion has previously been performed solely by Hadj-Rabia et al[3] in three patients. Our dental findings indicate impaired enamel formation to be a novel phenotype of HELIX syndrome. Indeed, amelogenesis imperfecta has previously been causally related to defects in claudin-16, -19, and -3.[34–36] Moreover, claudin-10 expression has been found in mature murine ameloblasts.[37]

We remark that all pathogenic *CLDN10* variants reported to date affect claudin-10b with the associated phenotype matching its bodily distribution. An impairment of claudin-10a function may thus not become clinically evident.

Regarding TAL ion transport in the absence of functional claudin-10b TJs, paracellular Na^+ reabsorption is expected to be markedly reduced while paracellular Ca^{2+} and Mg^{2+} transport via claudin-3/-16/-19 TJs should be enhanced.[33,38] These TJs are spatially separated from those comprised of claudin-10b and expand in its absence.[33] Our results from loop diuretic responsiveness testing suggest transcellular Na^+ transport to partially compensate for the defect in paracellular reabsorption. In addition, hydrochlorothiazide test results and secondary hyperaldosteronism suggest adaptive changes in the distal nephron, accounting for larger Na^+ transport capacities with concomitant K^+ secretion upon increased NaCl delivery. These mechanisms are well in line with limited salt-wasting on baseline. Pathophysiologically, defective TAL NaCl reabsorption has two major implications. First, it leads to renal NaCl wasting despite compensatory efforts, and second, it reduces the buildup of interstitial osmolality, accounting for hyposthenuria. The ensuing NaCl deficit in the extracellular fluid compartment induces metabolic alkalosis by volume contraction. Activation of the renin-angiotensin-aldosterone system following the reduction of effective arterial blood volume is implicated in maintaining the alkalotic state[39] and leads to the release of aldosterone which promotes a secondary KCl deficit. Hypokalemia in turn aggravates metabolic alkalosis.[40] Thus, in HELIX syndrome, metabolic alkalosis is caused by net deficits of NaCl and KCl.

Reduced buildup of interstitial osmolality in the renal medulla is consistent with the preserved renal aquaporin-2 response to desmopressin in another HELIX patient.[1] Prolonged thirsting unmasked a defective urine concentration mechanism in our patient, similar to previous results.[1] The defective urine concentration ability likely accounts for nocturnal enuresis in our patient. In particular, polyuria is unlikely to result from xerostomia which has been suggested previously.[3]

Given the above pathophysiological considerations, the question of suitable treatment options arises. Major goals

of medical therapy should be to ameliorate polyuria and to meet the imminent danger of acute-on-chronic hypokalemia. With defective claudin-10, long-term K^+ homeostasis appears to be achieved when plasma K^+ is low enough to limit urinary and exocrine K^+ losses to an amount that matches its input. Our data indicate that aggressive KCl substitution, therefore, is not expected to be of sustained benefit. Rather, mineralocorticoid receptor antagonists or blockers of the epithelial Na^+ channel (ENaC) should be employed.

Clearly, one drawback of our study is its confinement to the assessment of a single patient. However, this is only the sixth reported instance of a homozygous *CLDN10* variant associated with human disease and the fourth such variant affecting both protein isoforms.[1–5] In conclusion, we demonstrated that claudin-10a/b G163A/G165A causes a variation of HELIX syndrome based on defective claudin-10 TJ strand assembly. Thereby, claudin-10b is more severely affected than claudin-10a. Phenotypic traits result from the tissue-specific deficiency in insertion of aberrant claudin-10 into TJs, a process that may depend on the presence of other TJ components. Although both mutant isoforms are generally capable of forming paracellular channels with preserved electrophysiological properties if inserted into pre-existing TJs, their absolute TJ abundance may be reduced and thereby determine the degree of paracellular route dysfunction. Whether structural interference with claudin oligomerization constitutes a more general mechanism of pathogenicity in HELIX syndrome remains to be determined in future studies.

Author contributions

SS, DG, and JH conceived the study. SS, JP, and DG performed experiments. SS, JP, RS, and DG analyzed experimental data. SS performed clinical testing and analyzed the data. JP performed homology modeling. SS, SG, and AR contributed clinical data. SN and CB performed genetic analyses. SS wrote the manuscript, with contributions and editions from JP, DG, and JH. All authors approved the final version of the manuscript.

Conflict of interests

The authors declare no conflict of interests.

Funding

This work was supported by Deutsche Forschungsgemeinschaft (DFG) grants (No.GU 447/14-1, 14-2 to DG, PI 837/4-1, 4-2 to JP, and (No. HA 6908/2-1 to JH, respectively), and by Else Kröner-Fresenius-Stiftung grant (No. 2016_A52 to JH). JH receives additional funding from the DFG (No. 6908/3-1) and from the Fritz Thyssen Stiftung. CB is an employee of Limbach and holds a part-time faculty appointment at the University of Freiburg. His research laboratory receives support from the DFG (No. BE 3910/8-1 and BE 3910/9-1) and from the Federal Ministry of Education and Research (BMBF, No. 01GM1903I and 01GM1903G).

Acknowledgements

We wish to thank the patient featured in this study for his participation and continuing interest in our research regarding his syndrome and its treatment options. We would like to thank Luise Müller, Gabriele Kersten, Anja Fromm, and In-Fah Maria Lee for technical assistance.

Appendix A. Supplementary Data

Supplementary Data to this article can be found online at https://doi.org/10.1016/j.gendis.2021.06.006.

References

1. Bongers EMHF, Shelton LM, Milatz S, et al. A novel hypokalemic-alkalotic salt-losing tubulopathy in patients with *CLDN10* mutations. *J Am Soc Nephrol*. 2017;28(10):3118—3128.
2. Klar J, Piontek J, Milatz S, et al. Altered paracellular cation permeability due to a rare *CLDN10B* variant causes anhidrosis and kidney damage. *PLoS Genet*. 2017;13(7), e1006897.
3. Hadj-Rabia S, Brideau G, Al-Sarraj Y, et al. Multiplex epithelium dysfunction due to *CLDN10* mutation: the HELIX syndrome. *Genet Med*. 2018;20(2):190—201.
4. Meyers N, Nelson-Williams C, Malaga-Dieguez L, et al. Hypokalemia associated with a claudin 10 mutation: a case report. *Am J Kidney Dis*. 2019;73(3):425—428.
5. Alzahrani AS, Hussein M, Alswailem M, et al. A novel claudin-10 mutation with a unique mechanism in two unrelated families with HELIX syndrome. *Kidney Int*. 2021;100(2):415—429.
6. Van Itallie CM, Rogan S, Yu A, Vidal LS, Holmes J, Anderson JM. Two splice variants of claudin-10 in the kidney create paracellular pores with different ion selectivities. *Am J Physiol Renal Physiol*. 2006;291(6):F1288—F1299.
7. Günzel D, Stuiver M, Kausalya PJ, et al. Claudin-10 exists in six alternatively spliced isoforms that exhibit distinct localization and function. *J Cell Sci*. 2009;122(Pt 10):1507—1517.
8. Milatz S, Breiderhoff T. One gene, two paracellular ion channels-claudin-10 in the kidney. *Pflugers Arch*. 2017;469(1):115—121.
9. Günzel D, Yu ASL. Claudins and the modulation of tight junction permeability. *Physiol Rev*. 2013;93(2):525—569.
10. Krause G, Protze J, Piontek J. Assembly and function of claudins: structure-function relationships based on homology models and crystal structures. *Semin Cell Dev Biol*. 2015;42:3—12.
11. Claude P, Goodenough DA. Fracture faces of zonulae occludentes from "tight" and "leaky" epithelia. *J Cell Biol*. 1973;58(2):390—400.
12. Günzel D, Fromm M. Claudins and other tight junction proteins. *Compr Physiol*. 2012;2(3):1819—1852.
13. Hempel C, Protze J, Altun E, et al. Assembly of tight junction strands: claudin-10b and claudin-3 form homo-tetrameric building blocks that polymerise in a channel-independent manner. *J Mol Biol*. 2020;432(7):2405—2427.
14. Piontek J, Krug SM, Protze J, Krause G, Fromm M. Molecular architecture and assembly of the tight junction backbone. *Biochim Biophys Acta Biomembr*. 2020;1862(7):183279.
15. Fromm M, Piontek J, Rosenthal R, Günzel D, Krug SM. Tight junctions of the proximal tubule and their channel proteins. *Pflugers Arch*. 2017;469(7—8):877—887.
16. Lu H, Galeano MCR, Ott E, et al. Mutations in *DZIP1L*, which encodes a ciliary-transition-zone protein, cause autosomal recessive polycystic kidney disease. *Nat Genet*. 2017;49(7):1025—1034.

17. Colussi G, Bettinelli A, Tedeschi S, et al. A thiazide test for the diagnosis of renal tubular hypokalemic disorders. *Clin J Am Soc Nephrol*. 2007;2(3):454—460.
18. Fenske W, Refardt J, Chifu I, et al. A copeptin-based approach in the diagnosis of diabetes insipidus. *N Engl J Med*. 2018; 379(5):428—439.
19. Fiser A, Sali A. Modeller: generation and refinement of homology-based protein structure models. *Methods Enzymol*. 2003;374:461—491.
20. Suzuki H, Nishizawa T, Tani K, et al. Crystal structure of a claudin provides insight into the architecture of tight junctions. *Science*. 2014;344(6181):304—307.
21. Milatz S, Piontek J, Schulzke J-D, Blasig IE, Fromm M, Günzel D. Probing the *cis*-arrangement of prototype tight junction proteins claudin-1 and claudin-3. *Biochem J*. 2015;468(3):449—458.
22. Milatz S, Piontek J, Hempel C, et al. Tight junction strand formation by claudin-10 isoforms and claudin-10a/-10b chimeras. *Ann N Y Acad Sci*. 2017;1405(1):102—115.
23. Yu ASL, Cheng MH, Angelow S, et al. Molecular basis for cation selectivity in claudin-2-based paracellular pores: identification of an electrostatic interaction site. *J Gen Physiol*. 2009;133(1): 111—127.
24. Timper K, Fenske W, Kühn F, et al. Diagnostic accuracy of copeptin in the differential diagnosis of the polyuria-polydipsia syndrome: a prospective multicenter study. *J Clin Endocrinol Metab*. 2015;100(6):2268—2274.
25. Christ-Crain M, Bichet DG, Fenske WK, et al. Diabetes insipidus. *Nat Rev Dis Primers*. 2019;5(1):54.
26. Youn JH. Gut sensing of potassium intake and its role in potassium homeostasis. *Semin Nephrol*. 2013;33(3):248—256.
27. Ethier JH, Kamel KS, Magner PO, Lemann J, Halperin ML. The transtubular potassium concentration in patients with hypokalemia and hyperkalemia. *Am J Kidney Dis*. 1990;15(4):309—315.
28. Milatz S. A novel claudinopathy based on claudin-10 mutations. *Int J Mol Sci*. 2019;20(21):5396.
29. Piontek J, Winkler L, Wolburg H, et al. Formation of tight junction: determinants of homophilic interaction between classic claudins. *FASEB J*. 2008;22(1):146—158.
30. Rosenthal R, Milatz S, Krug SM, et al. Claudin-2, a component of the tight junction, forms a paracellular water channel. *J Cell Sci*. 2010;123(11):1913—1921.
31. Krug SM, Günzel D, Conrad MP, et al. Claudin-17 forms tight junction channels with distinct anion selectivity. *Cell Mol Life Sci*. 2012;69(16):2765—2778.
32. Rosenthal R, Günzel D, Piontek J, et al. Claudin-15 forms a water channel through the tight junction with distinct function compared to claudin-2. *Acta Physiol (Oxf)*. 2020;228(1):e13334.
33. Milatz S, Himmerkus N, Wulfmeyer VC, et al. Mosaic expression of claudins in thick ascending limbs of Henle results in spatial separation of paracellular Na^+ and Mg^{2+} transport. *Proc Natl Acad Sci U S A*. 2017;114(2):E219—E227.
34. Bardet C, Courson F, Wu Y, et al. Claudin-16 deficiency impairs tight junction function in ameloblasts, leading to abnormal enamel formation. *J Bone Miner Res*. 2016;31(3):498—513.
35. Bardet C, Ribes S, Wu Y, et al. Claudin loss-of-function disrupts tight junctions and impairs amelogenesis. *Front Physiol*. 2017; 8:326.
36. Yamaguti PM, Neves FdAR, Hotton D, et al. Amelogenesis imperfecta in familial hypomagnesaemia and hypercalciuria with nephrocalcinosis caused by *CLDN19* gene mutations. *J Med Genet*. 2017;54(1):26—37.
37. Hata M, Kawamoto T, Kawai M, Yamamoto T. Differential expression patterns of the tight junction-associated proteins occludin and claudins in secretory and mature ameloblasts in mouse incisor. *Med Mol Morphol*. 2010;43(2):102—106.
38. Breiderhoff T, Himmerkus N, Stuiver M, et al. Deletion of claudin-10 (*Cldn10*) in the thick ascending limb impairs paracellular sodium permeability and leads to hypermagnesemia and nephrocalcinosis. *Proc Natl Acad Sci U S A*. 2012;109(35): 14241—14246.
39. Liu F-Y, Cogan MG. Angiotensin II: a potent regulator of acidification in the rat early proximal convoluted tubule. *J Clin Invest*. 1987;80(1):272—275.
40. Kamel KS, Halperin ML. Metabolic alkalosis. In: *Fluid, Electrolyte, and Acid-Base Physiology: A Problem-Based Approach*. 5th ed. Amsterdam, AMS: Elsevier; 2017:171—197.
41. Sabandal MMI, Schäfer E. Amelogenesis imperfecta: review of diagnostic findings and treatment concepts. *Odontology*. 2016; 104(3):245—256.
42. Krause G, Winkler L, Mueller SL, Haseloff RF, Piontek J, Blasig IE. Structure and function of claudins. *Biochim Biophys Acta*. 2008;1778(3):631—645.